Monthly Notices
of the
ROYAL ASTRONOMICAL SOCIETY

MNRAS **462,** 858–866 (2016)
Advance Access publication 2016 July 19

doi:10.1093/mnras/stw1692

The circumstellar disc of FS Tau B – a self-consistent model based on observations in the mid-infrared with *NACO*

Florian Kirchschlager,[1]★ Sebastian Wolf[1] and David Madlener[2]

[1]*Institute of Theoretical Physics and Astrophysics, Kiel University, Leibnizstraße 15, D-24118 Kiel, Germany*
[2]*Max Planck Institute for Radio Astronomy, Auf dem Hügel 69, D-53121 Bonn, Germany*

Accepted 2016 July 12. Received 2016 July 12; in original form 2015 December 19

ABSTRACT

Protoplanetary discs are a byproduct of the star formation process. In the dense mid-plane of these discs, planetesimals and planets are expected to form. The first step in planet formation is the growth of dust particles from submicrometre-sized grains to macroscopic mm-sized aggregates. The grain growth is accompanied by radial drift and vertical segregation of the particles within the disc. To understand this essential evolutionary step, spatially resolved multi-wavelength observations as well as photometric data are necessary which reflect the properties of both disc and dust. We present the first spatially resolved image obtained with *NACO* at the *VLT* in the L_p band of the near edge-on protoplanetary disc FS Tau B. Based on this new image, a previously published *Hubble* image in *H* band and the spectral energy distribution from optical to millimetre wavelengths, we derive constraints on the spatial dust distribution and the progress of grain growth. For this purpose we perform a disc modelling using the radiative transfer code MC3D. Radial drift and vertical sedimentation of the dust are not considered. We find a best-fitting model which features a disc extending from 2 au to several hundreds au with a moderately decreasing surface density and $M_\mathrm{disc} = 2.8 \times 10^{-2}\,\mathrm{M}_\odot$. The inclination amounts to $i = 80^\circ$. Our findings indicate that substantial dust grain growth has taken place and that grains of a size equal to or larger than 1 mm are present in the disc. In conclusion, the parameters describing the vertical density distribution are better constrained than those describing the radial disc structure.

Key words: radiative transfer – planets and satellites: formation – protoplanetary discs – circumstellar matter – stars: individual: FS Tau B – stars: pre-main sequence.

1 INTRODUCTION

The multiple system FS Tau is located in the Taurus-Auriga star-forming region at a distance of 140 pc ± 20 pc (Elias 1978). FS Tau is a hierarchical triple-system, consisting of the narrow T-Tauri-binary FS Tau A (separation: 0.228–0.27 arcsec; Simon et al. 1992; Hartigan & Kenyon 2003) and the young stellar object (YSO) FS Tau B at a projected separation of ∼20 arcsec west. FS Tau A and FS Tau B are accompanied by a circumbinary and a circumstellar disc, respectively. The disc around FS Tau B is in the focus of this study. Alternative designations of FS Tau B are Haro 6-5B, HH 157, HBC 381, and IRAS 04189+2650.

The YSO has been classified as a Class I–II source (Lada 1987) and has lost most of its original surrounding shell (Yokogawa et al. 2001). The disc is highly inclined ($i \approx 67^\circ$–80°; Krist et al. 1998; Yokogawa et al. 2001) and obscures the central star at shorter wavelengths. Consequently, the disc appears as a bipolar nebula in the near-infrared (NIR), separated by an opaque band with a length of 3–4 arcsec (Padgett et al. 1999) and a position angle of 144°–150°. Since the disc is not orientated exactly edge-on and the dust particles potentially scatter non-isotropically, the two wings of the nebular structure differ in brightness. The disc mass has been constrained by several observations to $2 \times 10^{-3}\,\mathrm{M}_\odot$ to $4 \times 10^{-2}\,\mathrm{M}_\odot$ (Dutrey et al. 1996; Yokogawa et al. 2001, 2002). Based on the observed low accretion rate, an age of 3.6×10^5–2.4×10^6 yr has been deduced (Yokogawa et al. 2002). Moreover, the object features a bipolar jet with a perpendicular orientation towards the opaque band (Mundt et al. 1984).

Because of its low age and distance, FS Tau B is predestined to investigate the growth of dust grains in the context of planet formation. Due to its high inclination, the disc acts as a natural coronagraph reducing observational difficulties and artefacts common in coronagraphy. Furthermore, the vertical disc structure can be observed in the NIR without major disturbances by direct radiation from the stellar source. Comparable YSOs studied in the recent

★ E-mail: kirchschlager@astrophysik.uni-kiel.de

past are e.g. the Butterfly star IRAS 04302+2247 (Wolf, Padgett & Stapelfeldt 2003; Gräfe et al. 2013), CB 26 (Sauter et al. 2009), DG Tau B (Kruger et al. 2011), and HH 30 (Madlener et al. 2012).

Since the optical depth decreases in general with increasing wavelength, observations in the mid-infrared (MIR) allow the investigation of deeper regions of the disc and thus the study of thermal re-emission of warm dust closer to the mid-plane. In this context, spatially resolved multi-wavelength observations are required to reduce ambiguities in the data analysis which exist due to the lack of knowledge regarding the dust density, chemical composition, and grain size distribution. In addition, observations in the MIR potentially provide constraints for dust particles in deeper layers and thus for possible settling of larger grains (e.g. Pinte et al. 2008; Gräfe et al. 2013).

While hot dust and scattered stellar light can be readily observed at NIR wavelengths, spatially resolved MIR observations tracing warm dust are rare. This applies also to the system of FS Tau B which was observed with the *Hubble Space Telescope* (*HST*) in the optical and NIR domain (Krist et al. 1998; Padgett et al. 1999) and with lower resolution at millimetre wavelengths (Dutrey et al. 1996; Yokogawa et al. 2002).

The aim of this study is to investigate the density distribution of the protoplanetary disc of FS Tau B and to constrain the evolutionary stage of grain growth. We present a new observation in the L_p band ($\lambda = 3.74\,\mu$m) with ∼0.1 arcsec resolution (Section 2). Previously published observational data are summarized and presented in Section 3. The modelling campaign is based on the new observation in the MIR, a high resolution image obtained with *NICMOS/HST* in the NIR, and published photometry data (Section 4). The results are presented and discussed in Section 5.

2 OBSERVATION AND DATA REDUCTION

FS Tau B was observed in service mode on three nights in 2012 December and 2013 January [program no.: 090.C-0207(A), PI: F. Kirchschlager] with the *NACO* adaptive optics instrument, mounted on the UT4 at the *Very Large Telescope* (*VLT*, Lenzen et al. 2003; Rousset et al. 2003). The source was imaged with the L27-camera (pixel scale = 0.02712 arcsec pixel^{-1}) in the L_p band ($\lambda = 3.74\,\mu$m). The functions *Cube Mode* and *Auto-Jitter* were used within a square field with a side length of $\Delta\phi = 24$ arcsec. A single exposure lasted $t_B = 0.25$ s. For each detector position $N_B = 92$ single exposures were taken and the sum of detector positions for all three nights was $N_J = 112$. These settings yield a total integration time of $t_{total} = 2576\,s \approx 43$ min. The seeing during all observations was better than 1 arcsec and the relative airmass remained below 1.6. The *L*-band standard star FS 117 (B216-b9), located at an angular distance of 0.°5 from FS Tau B, was used as reference. This point-like source has $mag_L = 9.75$ mag ± 0.01 mag (Leggett et al. 2003).

The exposures were corrected for dark current and flat fielded. Bad pixels and cosmic ray artefacts were substituted by the median of the surrounding pixels, and all single exposures were added with respect to the jitter positions. The photometric calibration was performed by estimating the total count rates of the target and the reference star by using the average of all exposures. Different exposure times of the observations were taken into account. The total flux of FS Tau B in the L_p band amounts to $F_\nu = 53.6$ mJy ± 1.1 mJy. This value matches well with the course of the spectral energy distribution (SED; see Fig. 3). The uncertainty comprises the noise in the map of FS Tau B and FS 117 as well as the uncertainty of the flux of the reference star.

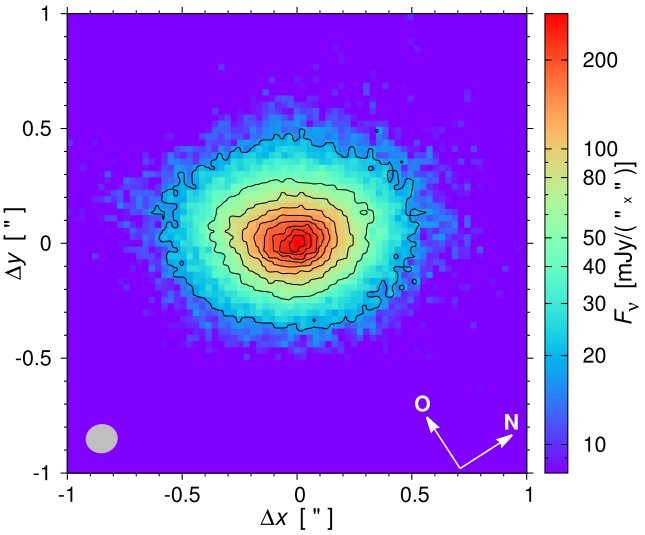

Figure 1. Map of FS Tau B taken with *NACO* in L_p band ($\lambda = 3.74\,\mu$m). The image was rotated by an angle of −57° in order to align the major axis of the elongated object with the horizontal image-axis. The contours correspond to flux densities in linear steps of 10 per cent, from 10 per cent to 90 per cent of the maximum flux density. The colour scale is logarithmic. The ellipse in the bottom left corresponds to the FWHM of the PSF. The position angle of the major axis of the PSF is PA = 155° ± 10°.

Table 1. Position angle PA of the disc plane of FS Tau B.

Position angle PA	Ref.	Note
144° ± 3°	Krist et al. (1998)	(1)
147°	Padgett et al. (1999)	(1)
138° ± 7°	Yokogawa et al. (2001)	(1)
147° ± 5°	this work	(1)
150° ± 10°	Yokogawa et al. (2002)	(2)
147° ± 8°	Gledhill, Warren-Smith & Scarrott (1986)	(3)

Notes. (1) PA of the dust disc; (2) PA of the gas disc; (3) PA corresponds to polarization angle in the optical wavelength range.

The reduced image was rotated by an angle of −57° in order to align the major axis of the object with the horizontal axis. The resulting map of FS Tau B in L_p band ($\lambda = 3.74\,\mu$m) is presented in Fig. 1 where the source appears as a single elongated object with a ratio of major to minor axis of 1.3. The object is centred on the pixel with peak flux density. The position angle of the major axis is PA = 147° ± 5°, a value that agrees well with literature data for the orientation of the disc plane (Table 1). Therefore, the major axis of the observed object is interpreted as the disc plane. The extension of the 10 per cent-contour line of ∼0.8 arcsec × 1 arcsec is smaller than in the NIR (Padgett et al. 1999).

Radial profiles were determined along the major and minor axis of the observed brightness distribution (Fig. 2). The FWHM for FS Tau B along the major axis is $x_{FWHM} = 0.29$ arcsec and for the minor axis $x_{FWHM} = 0.22$ arcsec while the FWHM for the radial profiles of the PSF are $x_{FWHM} = 0.135$ arcsec and 0.12 arcsec, respectively. Therefore, FS Tau B is spatially resolved in this L_p band observation. Left and right wing of the major/minor axis deviate by less than 0.03 arcsec, indicating only negligible asymmetry.

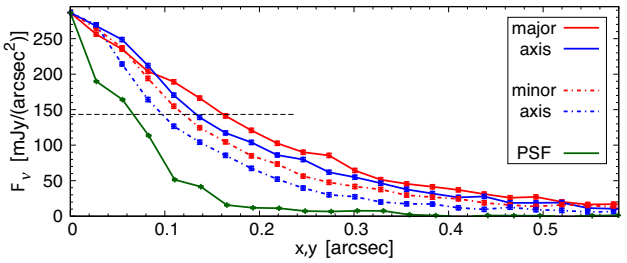

Figure 2. Radial profiles of the observation of FS Tau B in L_p band, centred on the pixel with maximum flux density. The flux densities as a function of distance x (y) are determined as cuts along the major (solid lines) and minor axis (dashed lines). The radial profile along the major axis of the PSF is scaled for comparison. The dashed horizontal line marks the half-maximum value to derive the FWHM.

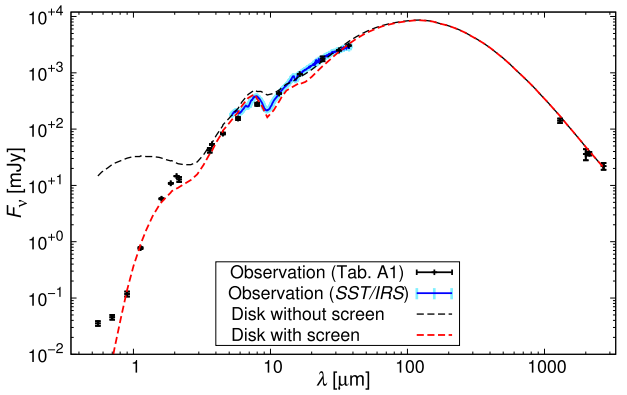

Figure 3. Photometric data of FS Tau B and the SED of the best-fitting model found in Section 5 (red dashed line). The black dashed line shows the SED of the same model without extinction screen ($A_V = 0$).

3 FURTHER OBSERVATIONS

For the modelling of the disc of FS Tau B, further observational data are required which are presented in this section.

3.1 Spectral energy distribution

The photometric data points are summarized in Table A1 in the appendix and plotted in Fig. 3. The data set from *Spitzer* (*IRS/SST*) contains 366 data points in the wavelength range from 5.2 μm to 37.9 μm. The known SED of FS Tau B comprises continuum fluxes from the optical up to the millimetre and radio range and shows some features.

(i) A disc with high inclination as seen on the NIR image (Padgett et al. 1999; Fig. 4) should cause higher fluxes in the scattering range of the SED compared to the maximum flux at wavelengths in the far-infrared. This is not the case for FS Tau B.

(ii) Thermal re-emission at MIR wavelengths suggests the presence of warm dust and therefore a small inner disc radius.

(iii) The *IRS/SST* data set shows an absorption feature which indicates the presence of crystalline silicate in the dust. Compared to other highly inclined discs (e.g. CB 26, HH 30, Butterfly star), the feature is less pronounced for FS Tau B.

(iv) The regression line for the (sub-)millimetre range of the SED is presented in Fig. 5. The slope has a value of $\alpha_{mm} = 2.6 \pm 0.2$ and is significantly smaller than in the case of dust in the interstellar medium (ISM; $\alpha_{mm} \sim 3.7$; Weingartner & Draine 2001) which suggests that grain growth has taken place in the disc (e.g. Natta et al. 2007). Moreover, when the regression also includes observed fluxes at $\lambda = 2$ cm and 6 cm, the slope reduces further to $\alpha'_{mm} = 2.0 \pm 0.2$. However, these observations might be contaminated by free–free-radiation of the jet (e.g. Marti, Rodriguez & Reipurth 1993; Pety et al. 2006).

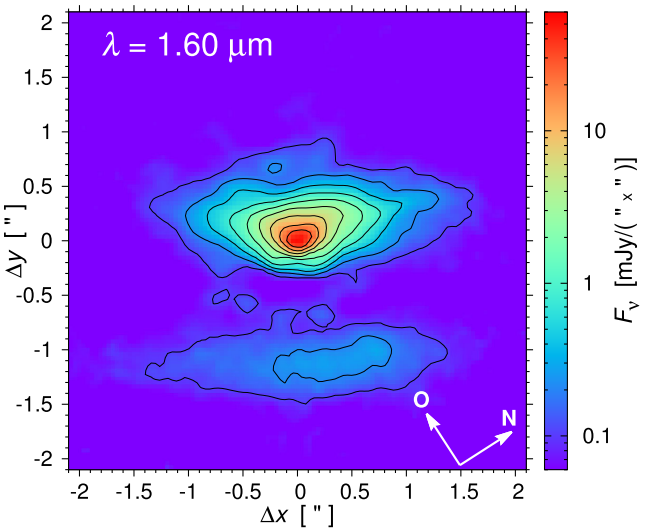

Figure 4. Map of FS Tau B taken with the *HST* in the *F*160*W*-filter ($\lambda = 1.60$ μm). The contours correspond to flux densities in linear steps of 10 per cent, from 10 per cent to 90 per cent of the maximum flux density. The colour scale is logarithmic (adopted from Padgett et al. 1999; private communication with W. Brandner).

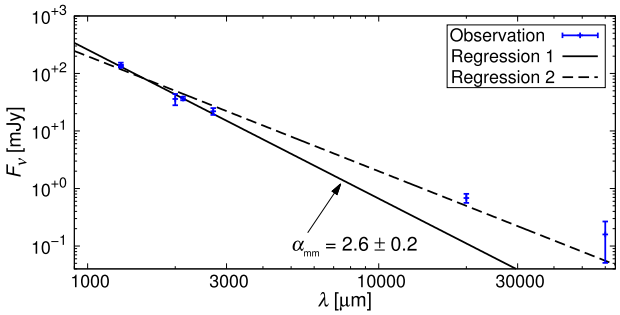

Figure 5. Spectral index for the disc of FS Tau B. The lines are determined using the method of least squares. If the fluxes in the centimetre range are neglected, the slope is $\alpha_{mm} = 2.6 \pm 0.2$ (solid line), otherwise $\alpha'_{mm} = 2.0 \pm 0.2$ (dashed line).

3.2 Observation in the near-infrared

FS Tau B was observed in the NIR with the NIC2 camera of the instrument *NICMOS/HST* on 1997 October 29, (Padgett et al. 1999) in the filters *F*110*W*, *F*160*W*, *F*187*W*, and *F*205*W* (instrument description: Thompson et al. 1998). The detailed data reduction procedure is described in Padgett et al. (1999). The object is seen in the maps as a bipolar nebula. The bipolar appearance decreases with increasing wavelength which is consistent with our observation in L_p band where only a single lobe can be seen (Fig. 1). In Fig. 4 the image at $\lambda = 1.60$ μm taken from Padgett et al. (1999) is presented which was used for modelling in the following section.

4 DISC MODELLING

In this section our approach to reproduce the appearance of the protoplanetary disc of FS Tau B is discussed. In the following, the applied software, the disc and dust model, as well as the modelling procedure are introduced.

4.1 Radiative transfer

We used the program MC3D for our radiative transfer simulations which is based on the Monte Carlo method (Wolf, Henning & Stecklum 1999; Wolf 2003a). The code implements the temperature-correction technique described by Bjorkman & Wood (2001), the absorption concept of Lucy (1999), and the scattering scheme by Cashwell & Everett (1959). The radiation field is described by the Stokes formalism (I, Q, U, V; Stokes 1852; Chandrasekhar 1946). The software first simulates the temperature distribution and then uses this information to calculate the SED, as well as spatially resolved scattering and re-emission maps for the given dust density distribution.

4.2 Model for FS TAU B

Our chosen model consists of three components. The central star, a flared circumstellar disc and an extinction screen between the system and the observer. Observations in the millimetre domain by Yokogawa et al. (2001) and synthetic imaging in the NIR by Stark et al. (2006) showed that FS Tau B already lost the shell which enveloped the disc during the earliest stages. Therefore, a shell is not considered in our modelling approach of FS Tau B.

The disc is heated by a source which is assumed to be a blackbody, characterized by its effective temperature $T_{\rm heat}$ and radius $R_{\rm heat}$, resulting in a corresponding luminosity $L_{\rm heat}$. Both quantities ($T_{\rm heat}$, $R_{\rm heat}$) were varied during the modelling process. The heating source is composed of the central star and further contributions such as viscous friction and accretion shocks.

For the density distribution we adopt the canonical flared disc parametrization that depends on the radial distance from the star and the distance from the disc mid-plane (Shakura & Sunyaev 1973),

$$\rho(R,z) = \rho_0 \left(\frac{R}{R_{100}}\right)^{-\alpha} \exp\left(-\frac{1}{2}\left[\frac{z}{h(R)}\right]^2\right). \quad (1)$$

Here, R is the cylindrical distance from the centre and z the distance from the disc mid-plane. The factor ρ_0 fixes the total disc mass given the radial boundaries. The scale height

$$h(R) = h_{100}\left(\frac{R}{R_{100}}\right)^{\beta} \quad (2)$$

encodes the flaring of the disc. The inner and outer radius $R_{\rm in}$ and $R_{\rm out}$, the geometrical parameters α and β, the scale height h_{100} at the reference radius $R_{100} = 100$ au as well as the dust mass $M_{\rm dust}$ are in total six free parameters.

FS Tau B is located in the Taurus-Auriga star-forming region and surrounded by a complex accumulation of material. To take the ISM into account as a source of extinction, we adopt an extinction screen between disc and observer which attenuates the radiation of the object as a function of wavelength, see Fig. 6. A further motivation lies in our finding that the SED cannot be reproduced by a highly inclined disc ($i > 60°$) without an extinction screen ($A_V = 0$). The extinction properties of interstellar dust grains are assumed for this screen and its thickness is characterized by the optical extinction $A_V \approx 1.086\,\tau_V$ where τ_V denotes the optical depth in V band ($\lambda = 0.548$ μm). The observables calculated by radiative transfer are modified by the wavelength dependent absorption of the screen. In Section 5 we show that thermal reemission from the extinction screen is negligible.

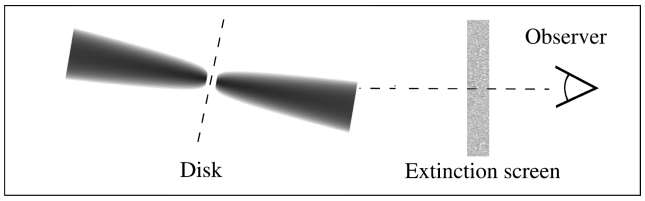

Figure 6. Position of the extinction screen between disc and observer.

The distance towards FS Tau B corresponds to the distance of the Taurus-Auriga star-forming region at $d = 140\,\mathrm{pc} \pm 20\,\mathrm{pc}$. The disc inclination i is treated as another free parameter.

4.3 Dust model

The dust grains in our disc model are assumed to be spherical and composed of 62.5 per cent astronomical silicate and 37.5 per cent crystalline graphite with a total bulk density of $\rho = 2.7\,\mathrm{g\,cm^{-3}}$ (Weingartner & Draine 2001). The dust grains follow the size distribution $\mathrm{d}n \propto a^{-q}\,\mathrm{d}a$ with exponent $q = 3.5$ (Mathis, Rumpl & Nordsieck 1977) with grain radii varying in the interval $a \in [5\,\mathrm{nm},\ a_{\rm max}]$. Since the spectral index already indicates the presence of larger particles than found in the ISM, six discrete values for the maximum grain radius are considered: $a_{\rm max} = 0.25$ μm, 1 μm, 5 μm, 20 μm, 100 μm, and 1 mm. A spatial variation of grain size properties driven by segregation processes like dust settling is not considered. The optical properties of the particles are calculated with the program `miex` which is based on the theory of Mie-scattering (Mie 1908; Wolf & Voshchinnikov 2004). To reduce computational time and memory requirements for radiative transfer simulations, we applied the approximation by Wolf (2003b) which replaces the optical properties of a single grain with radius a by the weighted mean of optical properties for the entire grain population.

4.4 Quality of the fit

To search for the best-fitting model we have to compare the simulated quantities to the observational data. Therefore, we use the concept of χ^2 minimization with

$$\chi^2 \propto \left(\chi^2_{\rm SED} + \sum_{k=1}^{N} g_k\,\chi^2_k\right), \quad (3)$$

where $\chi^2_{\rm SED}$ and χ^2_k are the individual contributions of the SED and the kth of N maps, weighted with g_k, respectively. Here, $N = 2$ as we consider two maps at $\lambda = 1.60$ μm and 3.74 μm. For both, only the radial profiles along the major and minor axes are taken into account. Each flux of the SED and brightness profiles are normalized by dividing the difference between observed and modelled flux with their individual uncertainties. The maps are equally weighted ($g_1 = g_2$) and the g_k are chosen in a way that $\chi^2_{\rm SED}$ and the sum of the contributions of the two maps get in balance.

4.5 Modelling strategy

The parameter space of the described model is 11-dimensional. All parameters and their ranges are presented with the values for the

Table 2. Parameter space and values of the best-fitting model.

Parameter		Parameter space	Best-fitting model
$R_{\rm in}$	[au]	0.1–10	$2.0^{+1.2}_{-0.3}$
$R_{\rm out}$	[au]	150–400	$350^{+\ 50}_{-150}$
h_{100}	[au]	5–25	$10^{+\ 2}_{-1}$
α		1.0–4.0	$2.1^{+0.5}_{-0.6}$
β		1.0–2.0	$1.20^{+0.06}_{-0.01}$
$M_{\rm dust}$	[$M_\odot$]	10^{-6}–10^{-2}	$\left(2.8^{+0.3}_{-0.7}\right) \times 10^{-4}$
$a_{\rm max}$	[μm]	0.25–1000	1000
i	[°]	60–90	80^{+1}_{-2}
$A_{\rm V}$		0–20	12
$T_{\rm heat}$	[K]	3000–8000	7000^{+500}_{-600}
$R_{\rm heat}$	[$R_\odot$]	0.8–3.5	$2.1^{+0.4}_{-0.5}$

best-fitting model in Table 2. The chosen intervals are based on restrictions by observational data and modelling of similar objects (e.g. Sauter et al. 2009; Gräfe et al. 2013).

First the temperature distribution is calculated for each parameter set, then the SED and the scattering- and reemission maps for $\lambda = 1.60\,\mu$m and 3.74 μm are generated. The maps are convolved with an elliptical Gaussian function and the radial profiles are extracted along the major and minor axis. The simulated quantities are then compared to the observations and χ^2 is calculated according to equation (3).

The parameters i and A_V are not affected by the results of the radiation transport simulations and can thus be altered subsequently. The remaining parameters span a nine-dimensional parameter space. In order to find a model that reproduces most of the observational data, the method of Sauter et al. (2009) is applied and the parameters are fitted iteratively. At first the range of an individual parameter is sampled in four coarse steps. Then the two best values are selected and the procedure is continued to the next parameter. This sequence is repeated several times using random parameter order. The stepping of each parameter is refined in a smaller range in each sequence, based on the results of the previous sequence. The procedure ends when a sequence delivers no better model.

The uncertainties of each parameter are calculated by determining the range this parameter can be altered without exceeding the χ^2 of the best-fitting model by more than 10 per cent. There is no mathematical reason supporting this value, but its applicability has been proven within our study because deviations larger than 10 per cent generally give inferior results. The confidence intervals determined with this approach are unsymmetrical unlike the usual 1σ-interval.

5 RESULTS

The resulting best-fitting model reproduces the key characteristics of the observational data (Table 2). The following sections discuss the parameters of the best-fitting model (Section 5.1), the simulated SED (Section 5.2, Fig. 3), brightness maps (Section 5.3, Fig. 8) and the temperature distribution in the disc mid-plane (Section 5.4).

5.1 Disc parameters

In this section, the disc parameters of the best-fitting model are discussed separately.

The inner edge of the disc, as seen in thermal MIR emission maps, amounts to $R_{\rm in} = 2.0^{+1.2}_{-0.3}$ au, indicating the disc has no extended inner hole as observed for several other objects (e.g. Andrews et al. 2011; Gräfe et al. 2011). For the given central object, the sublimation radius is $R_{\rm sub} \approx 0.35$ au (Whitney et al. 2004). The high MIR fluxes imply the presence of warm dust located relatively close to the star.

Due to the low signal-to-noise ratio in the outer regions, the outer radius $R_{\rm out} = 350^{+50}_{-150}$ au is only weakly constrained. The studies of Krist et al. (1998), Padgett et al. (1999), Yokogawa et al. (2001), and Stark et al. (2006) obtained comparable values between 240 au and 309 au for the outer radius.

The scale height at $R_{100} = 100$ au, $h_{100} = 10^{+2}_{-1}$ au, the radial exponent $\alpha = 2.1^{+0.5}_{-0.6}$, and the flaring exponent $\beta = 1.20^{+0.06}_{-0.01}$ are typical for a protoplanetary disc (e.g. IM Lupi, Pinte et al. 2008; CB 26, Sauter et al. 2009). In addition, the criterion $\alpha = 3(\beta - \frac{1}{2})$ from viscous accretion theory is fulfilled (Shakura & Sunyaev 1973). The exponent of the surface density distribution, $p = \alpha - \beta = 0.9^{+0.5}_{-0.6}$, is consistent with theoretical (e.g. Bell et al. 1997) and empirical studies (e.g. Kitamura et al. 2002; Andrews & Williams 2007) which find $0.5 \lesssim p \lesssim 1$, indicating an monotonically decreasing density towards the outer edge. The surface density amounts to $\Sigma = 16.3\,{\rm g\,cm^{-2}}$ and $\Sigma = 1.1\,{\rm g\,cm^{-2}}$ at the distances $R = 5$ au and 100 au, respectively.

The total dust mass in the disc is determined to $M_{\rm dust} = 2.8^{+0.3}_{-0.7} \times 10^{-4}\,M_\odot$, assuming compact, spherical, and homogenous dust particles. If the canonical value of $M_{\rm gas}/M_{\rm dust} = 100$ is adopted (e.g. Hildebrand 1983), we derive a total mass of $\sim 2.8 \times 10^{-2}\,M_\odot$. This value is in agreement with Dutrey et al. (1996), Krist et al. (1998), Yokogawa et al. (2002), and Stark et al. (2006), who obtained values for the total disc mass ranging from $M_{\rm dust} = 1 \times 10^{-2}\,M_\odot$ to $4 \times 10^{-2}\,M_\odot$. Moreover, the criterion found by Toomre (1964) for a rotating disc indicates that the disc is gravitationally stable at all disc radii ($Q_{\rm T} > 1$).

The maximum grain radius of the best-fitting model is $a_{\rm max} = 1$ mm, more than three orders of magnitude larger than the maximum grain radius of the ISM (Mathis et al. 1977). We therefore conclude that grain growth has taken place in the disc of FS Tau B. Large particles radiate effectively in the (sub-)millimetre wavelength range and shape the slope in this range (Fig. 5). Since the next lower value in the parameter study is significantly smaller (100 μm), $a_{\rm max}$ is fixed to 1.0 mm and no uncertainties for this parameter are given. Although the derived value for the maximum grain radius is at the edge of the considered parameter space, the presence of larger dust particles cannot be deduced, as their effect on the observed SED is minor.

The inclination i is constrained by the SED and the radial brightness profiles to $i = 80^{\circ\,+1^\circ}_{-2^\circ}$. This value is consistent with the edge-on orientation deduced from the NIR maps. Krist et al. (1998), Padgett et al. (1999), Yokogawa et al. (2001), and Stark et al. (2006) found inclinations ranging from $i = 67^\circ$ up to 80°.

The central star has a spectral type of K5 ± 2 (White & Hillenbrand 2004) which corresponds to a stellar temperature of $T_\star = 4400^{+400}_{-400}$ K. Using evolutionary tracks of pre-main-sequence stars (Siess, Dufour & Forestini 2000), a stellar mass of $M_\star = 1.0\,M_\odot$ to $1.4\,M_\odot$ can be derived. With a temperature $T_{\rm heat} = 7000^{+500}_{-600}$ K and radius $R_{\rm heat} = 2.1^{+0.4}_{-0.5}$ au, we deduce a luminosity $L_{\rm heat} = 9.5^{+2.9}_{-3.5}\,L_\odot$ for the heating source. If we assume that the derived best-fitting luminosity $L_{\rm heat}$ is composed of contributions from the central star ($L_\star$) and accretion ($L_{\rm acc}$) only, we can derive the mass accretion rate using the relationship $L_{\rm acc} = \frac{G\,M_\star}{2\,R_\star}\frac{{\rm d}M}{{\rm d}t}$, where G is the gravitational constant. The mass accretion rate is then constrained to the interval

$3.2 \times 10^{-7}\,M_\odot\,yr^{-1}$–$1.2 \times 10^{-6}\,M_\odot\,yr^{-1}$ which is comparable to previous studies ($9.3 \times 10^{-8}\,M_\odot\,yr^{-1}$–$6.2 \times 10^{-7}\,M_\odot\,yr^{-1}$; Yokogawa et al. 2002).

The optical extinction A_V is very sensitive to other parameters such as the inclination, disc mass or inner radius. Since the uncertainty of this parameter is dominated by the variation of other parameters, the errors are not specified. In a fitting approach considering only the SED, models without extinction screen ($A_V = 0$) can reproduce the SED very well. However, the inclination in these parameter sets is only 40°–50°, thus contradicting information from observed images. On the other hand, a highly inclined disc yields a SED with larger fluxes than observed at wavelengths up to several micrometres. Following Sauter et al. (2009), an extinction screen with $A_V = 12$ is introduced which causes a wavelength-dependent reduction of these fluxes. The screen is optically thin at (sub-)millimetre wavelengths ($\tau_{1.3\,mm} \approx 8 \times 10^{-5}$). If we assume a dust temperature of ∼20 K in the screen, the resulting flux amounts to $F_\nu(\lambda = 1.3\,mm) \approx 2$ mJy, two magnitudes lower than the observed flux. Thus, the thermal reemission of the extinction screen can be neglected.

In summary it can be concluded that parameters which describe the vertical density distribution (β, h_{100}) of the disc are better restricted than those influencing the radial disc structure (R_{in}, R_{out}, α).

5.2 Spectral energy distribution

The photometry of the best-fitting model agrees well with the observational data from the MIR to millimetre wavelengths (Fig. 3). The SED shows the characteristic silicate absorption feature at ∼10 μm which is slightly more pronounced in the modelling than in the IRS data set. Since the flux in this band is in general very sensitive to changes in disc opacity, a small modification of dust properties, mass, or inclination influences the strength of the band. The simulated fluxes at wavelengths in the MIR beyond the silicate feature are lower than observations, showing deviations up to 40 per cent. The millimetre data and in particular the spectral index are reproduced quite well. The largest deviations occur at the shortest wavelengths, i. e. in the optical and NIR. Obviously, the fluxes of the model without extinction screen are too high in this wavelength range. The SED of the model with extinction screen shows a much higher conformity with the observational data. However, the slope in the optical range is too steep and the simulated fluxes at $\lambda = 0.55$ μm and 0.7 μm are lower than the observational data. In particular, the flux at $\lambda = 0.55$ μm cannot be explained by the model.

The percentage of scattered stellar radiation and thermal dust reemission is presented in Fig. 7 as a function of wavelength. Thermal reemission comprises radiation emitted and possibly scattered by dust grains. Increasing wavelength leads to reduced scattering, thus thermal reemission dominates at wavelengths $\lambda \gtrsim 3$ μm. Therefore, the NIR maps of the *HST* consist almost entirely of scattered stellar radiation, while the new *NACO* observation at $\lambda = 3.74$ μm (Fig. 1) contains 80 per cent thermal reemission according to our results.

5.3 Simulated maps and radial profiles

The synthetic images and their corresponding cuts at $\lambda =$ 1.10 μm, 1.60 μm, 1.87 μm, 2.05 μm, and 3.74 μm are compiled in Fig. 8. Apart from asymmetries which cannot be reproduced by the radially symmetric approach of the chosen model, the maps are comparable to the observations.

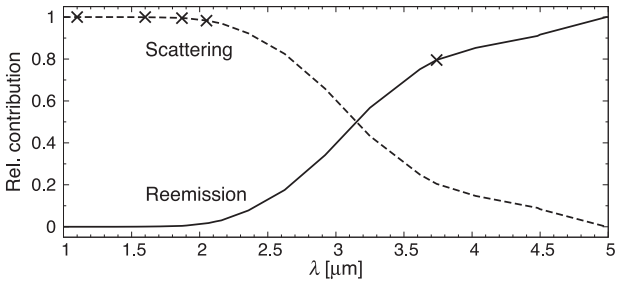

Figure 7. Relative contribution of scattered and re-emitted radiation to the total intensity of the best-fitting model (Table 2). The wavelengths of the observed/modelled NIR and MIR maps are marked at the dominating radiation source.

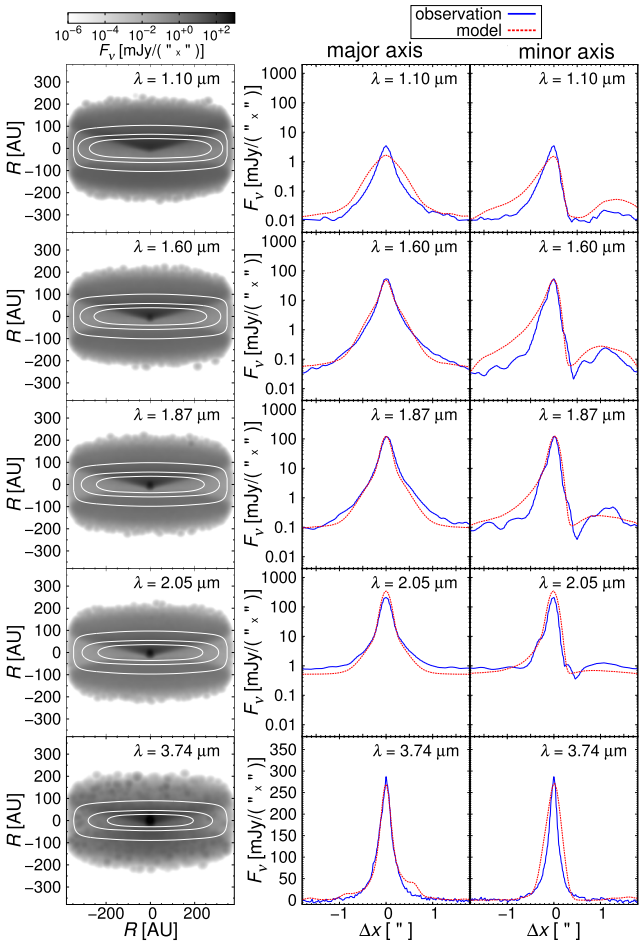

Figure 8. Left: synthetic images of the best-fitting model of FS Tau B at five wavelengths λ. The solid lines show the surfaces at which the optical depth for an outside observer takes the values $\tau_\lambda = 1, 5$, and 10, respectively. Middle and right: corresponding radial profiles of FS Tau B. The cuts were taken along the major and minor axis. For details see Section 5.3.

The profiles along the major axis are well reproduced by the model. Only the simulated profile of the shortest wavelength $\lambda = 1.10$ μm appears significantly wider than its observational counterpart. The profiles along the minor axis exhibit much larger deviations. The observations show a global maximum and a

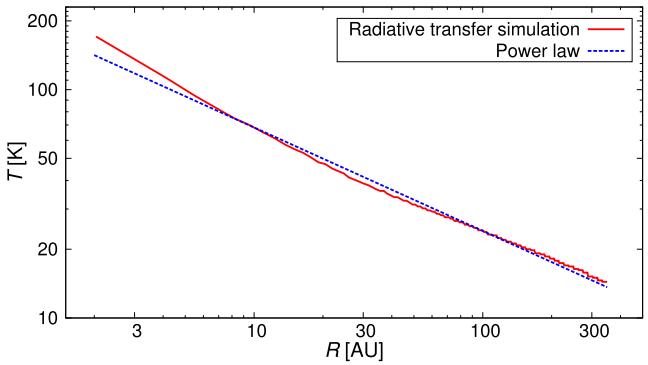

Figure 9. Temperature T in disc mid-plane as a function of the disc radius R for the best-fitting model. The red solid line shows the temperature determined in the radiative transfer simulations and the blue dashed line is the fitting by a power law $T(R) = T_{100}\left(\frac{R}{100\,\mathrm{au}}\right)^{-q}$ with $T_{100} = 24.44\,\mathrm{K} \pm 0.07\,\mathrm{K}$ and $q = 0.450 \pm 0.002$.

secondary local maximum, separated by an opaque band in the form of a local minimum. The contrast between the secondary maximum and the minimum of the simulated profiles cannot be reproduced, similar to the modelling of HH 30 (Cotera et al. 2001; Madlener et al. 2012). Apart from $\lambda = 1.10\,\mu\mathrm{m}$, the minimum of the observed profiles is more pronounced than for the simulated profiles. This phenomenon might reveal a systematic deviation of our model from reality. One explanation for this discrepancy lies in a gas and dust stream driven by the central jet which substantially enhances the scattered stellar radiation in this region and hence the contrast (e.g. Pety et al. 2006).

An increase of the wavelength results in a decrease of contrast until it vanishes at the longest wavelength. The contrast at the shortest wavelength $\lambda = 1.10\,\mu\mathrm{m}$ is low and contrary to the trend. Our model can not explain this observation.

A way to improve the prediction is to modify the underlying dust distribution. In particular a spatial variation of the particle size, caused by dust settling and segregation of large dust particles, has a strong influence on the local chromaticity and thus on scattered and re-emitted radiation from the disc (e.g. Pinte et al. 2008; Liu et al. 2012; Gräfe et al. 2013).

5.4 Mid-plane temperature

Fig. 9 shows the calculated temperature in the disc's mid-plane for the best-fitting model. The temperature varies from ∼15 K in the outer regions up to ∼200 K at the disc's inner edge. A power law

$$T(R) = T_{100}\left(\frac{R}{R_{100}}\right)^{-q} \tag{4}$$

is used to fit the temperature beyond 4 au. Using the method of least squares, we derive the values $T_{100} = 24.44\,\mathrm{K} \pm 0.07\,\mathrm{K}$ and $q = 0.450 \pm 0.002$. Moreover, the dust mass mean temperature in the disc is $\langle T_{\mathrm{dust}} \rangle = 26.7\,\mathrm{K}$. Because the relative deviation of the fit from the simulated distribution is smaller than 10 per cent for radii $R > 4$ au, the power law represents the simulated temperature quite well. In contrast, at radii below 4 au the temperature shows a steeper slope which can also be observed for other objects (e.g. HH 30, Madlener et al. 2012). This inner region is heated in our model by the protostar and the hot inner edge, i. e. NIR and MIR radiation provides a contribution to the heating. This is not the case at larger distances, causing the reduction of the temperature slope at several au.

Yokogawa et al. (2001) determined the values $T_{100} = 19.76\,\mathrm{K}$ and $q = 0.61$ which results in a steeper temperature slope. However, a different dust opacity and simpler disc geometry was used in their modelling campaign and only the SED was fitted.

5.5 Discussion

In this section we discuss constraints on several disc parameters by the observational data.

The disc inclination is limited by the photometry from 1 to 50 μm and the shape of the radial brightness profiles of all five maps. The inclined disc does not only shield the stellar scattered radiation by itself, as this scenario yields too high fluxes at optical wavelengths. Only a model of a highly inclined disc combined with an extinction screen yields optical/NIR fluxes of the same order as the observations. Because of the dependence on both SED and shape of the brightness profiles, the inclination depends only weakly on the value of A_{V}. Indeed, the quantity A_{V} is only constrained by observations in the wavelength range $0.5-3\,\mu\mathrm{m}$.

Because of the high inclination and optical depth, the radial disc structure (R_{in}, R_{out}, α) is not as well constrained as the vertical density distribution (β, h_{100}). In particular, the outer radius of several hundreds au has a large uncertainty interval because it is not traced by the NIR and MIR maps and only weakly by (sub-)millimetre photometry. Instead, resolved interferometric observations at (sub-)millimetre wavelengths are needed to constrain the outer radius.

The spectral index by itself indicates the presence of large particles. Furthermore, the wavelength range $1-3\,\mu\mathrm{m}$ yields too low fluxes in the scattering regime if only submicrometre particles are considered. Since this influences the profiles in the NIR, the maps constrain the maximum grain radius as well. The scattered fraction for the MIR map is only 20 per cent of the total flux, thus the impact of this map on the maximum grain radius is smaller. The dust mass, however, influences mostly the (sub-)millimetre wavelength domain and the depth of the silicate band.

The geometric parameters describe the spatial distribution of the material which emits at wavelengths beyond the NIR. Therefore, observations in the MIR are important because the contribution of the dust component becomes comparable to or greater than the protostar. The L_{p} image shows that the emitting material is located close to the centre, thereby putting a limit on the inner radius. The asymmetry of the Lp image is below its spatial resolution. At shorter wavelengths, the inner edge is not directly visible, as can be seen from the asymmetry of the NIR maps, while the MIR map is more symmetrical.

The settling of larger grains is not considered in the modelling but might have a strong influence on the scattered and re-emitted radiation from the disc (e.g. Pinte et al. 2008; Liu et al. 2012) and thus also on disc parameters. In particular, Gräfe et al. (2013) found in the case of the Butterfly star IRAS 04302+2247 a reduction of the scale height h_{100} and steeper slopes of the radial (sub-)millimetre profiles. The decreased incidence of larger grains with several μm diameter in upper disc layers leads to a reduction of scattered radiation in the wavelength range of a few μm and consequently also on the optical extinction A_{V}. In general, the short-wavelength range and the slopes of the radial profiles are affected by dust settling, while the influence at millimetre wavelengths is minor.

6 CONCLUSION

In this paper a spatially resolved observation of FS Tau B obtained with the instrument *NACO/VLT* in the MIR (L_{p} band, $\lambda = 3.74\,\mu\mathrm{m}$)

was presented. Based on this new image, previously published photometry, and a spatially resolved observation in the NIR taken with *NICMOS/HST*, a parameter study was performed which resulted in new constraints for the disc parameters. The main observables are reproduced satisfactorily by the best-fitting model.

The disc extends from an inner radius at $R_{\rm in} = 2$ au to an outer radius of several hundreds au. The values for the scale height at radius $R_{100} = 100$ au, $h_{100} = 10^{+2}_{-1}$ au, and the geometrical parameters $\alpha = 2.1^{+0.5}_{-0.6}$ and $\beta = 1.20^{+0.06}_{-0.01}$ are found to be in the typical range for protoplanetary discs. Moreover, the surface density decreases moderately with $p = 0.9^{+0.5}_{-0.6}$. In summary, parameters describing the vertical density distribution (β, h_{100}) of the disc are better constrained than those influencing the radial disc structure ($R_{\rm in}$, $R_{\rm out}$, α). The temperature in the mid-plane at $R = 100$ au has a value of $T_{100} \approx 24$ K.

The dust mass is determined to $M_{\rm dust} = 2.8 \times 10^{-4}\,{\rm M}_\odot$. Assuming the canonical ratio of gas to dust, $M_{\rm gas}/M_{\rm dust} = 100$ (e.g. Hildebrand 1983), we derive a total disc mass of $M_{\rm disc} = 2.8 \times 10^{-2}\,{\rm M}_\odot$. Evaluation of Toomre's criterion suggests gravitational stability throughout the disc. To reproduce the observational data much larger dust grains ($a_{\rm max} = 1$ mm) than primordial particles of the ISM are needed. The spectral index $\alpha_{\rm mm} \approx 2.6$ implies the presence of larger dust particles and therefore grain growth in the disc. The inclination $i = 80^\circ$ is constrained by a combination of SED and images, and an extinction screen in the foreground with an optical extinction of $A_{\rm V} = 12$ gives the best results. The heating source in our best-fitting model has a luminosity of $L_\star \approx 9.5\,{\rm L}_\odot$. The mass accretion rate is derived to $3.2 \times 10^{-7}\,{\rm M}_\odot\,{\rm yr}^{-1}$–$1.2 \times 10^{-6}\,{\rm M}_\odot\,{\rm yr}^{-1}$.

The observed SED is well reproduced by the presented best-fitting model. While the NIR maps observed with *NICMOS/HST* consist almost entirely of scattered stellar radiation, the MIR observation is dominated (∼80 per cent) by thermal reemission. The simulated maps show a highly inclined disc. The radial profiles along the major axis are well reproduced, whereas the deviations on the minor axis are larger.

The modelling is based on spatially resolved NIR and MIR observations. The decreased optical depth in the MIR reveals slightly deeper embedded regions and potentially larger particles which settled towards the disc mid-plane and moved closer to the central star. In our study we need the presence of larger particles for the modelling but the resolution of the MIR map is too low to get hints for dust settling or to exclude the occurrence of larger particles in the disc's surface regions.

In general, observations at longer wavelengths probe larger grain sizes and deeper disc regions. Therefore, future studies have to verify the presented model by taking into account observations in the far-infrared and at (sub-)millimetre wavelengths. In addition, the spatial variation of particle size within the disc and thus the spatial dependency of the spectral index can be investigated with observations at these wavelengths. *ALMA*, the largest (sub-)millimetre interferometer (e.g. Boley et al. 2012) and other high resolution and sensitive observatories, such as the planned *JWST* (e.g. Mather 2010), will enable us to investigate the disc of FS Tau B with increased sensitivity on smaller scales, and to obtain a better understanding of disc evolution in general.

ACKNOWLEDGEMENTS

FK acknowledges financial support by the German Research Foundation (*Deutsche Forschungsgemeinschaft, DFG*) through the project WO 857/7-1. We wish to thank Yao Liu.

REFERENCES

Andrews S. M., Williams J. P., 2007, ApJ, 659, 705
Andrews S. M., Wilner D. J., Espaillat C., Hughes A. M., Dullemond C. P., McClure M. K., Qi C., Brown J. M., 2011, ApJ, 732, 42
Bell K. R., Cassen P. M., Klahr H. H., Henning T., 1997, ApJ, 486, 372
Bjorkman J. E., Wood K., 2001, ApJ, 554, 615
Boley A. C., Payne M. J., Corder S., Dent W. R. F., Ford E. B., Shabram M., 2012, ApJ, 750, L21
Brown A., Drake S. A., Mundt R., 1986, in Zeilik M., Gibson D. M., eds, Lecture Notes in Physics, Vol. 254, Cool Stars, Stellar Systems and the Sun. Springer-Verlag, Berlin, p. 451
Cashwell E., Everett C., 1959, A Practical Manual on the Monte Carlo Method for Random Walk Problems. Pergamon Press, London
Chandrasekhar S., 1946, ApJ, 104, 110
Connelley M. S., Reipurth B., Tokunaga A. T., 2007, AJ, 133, 1528
Cotera A. S. et al., 2001, ApJ, 556, 958
Dutrey A., Guilloteau S., Duvert G., Prato L., Simon M., Schuster K., Menard F., 1996, A&A, 309, 493
Elias J. H., 1978, ApJ, 224, 857
Furlan E. et al., 2011, ApJS, 195, 3
Gledhill T. M., Warren-Smith R. F., Scarrott S. M., 1986, MNRAS, 223, 867
Gräfe C., Wolf S., Roccatagliata V., Sauter J., Ertel S., 2011, A&A, 533, A89
Gräfe C., Wolf S., Guilloteau S., Dutrey A., Stapelfeldt K. R., Pontoppidan K. M., Sauter J., 2013, A&A, 553, A69
Hartigan P., Kenyon S. J., 2003, ApJ, 583, 334
Hildebrand R. H., 1983, QJRAS, 24, 267
Kitamura Y., Momose M., Yokogawa S., Kawabe R., Tamura M., Ida S., 2002, ApJ, 581, 357
Krist J. E. et al., 1998, ApJ, 501, 841
Kruger A. J., Richter M. J., Carr J. S., Najita J. R., Doppmann G. W., Seifahrt A., 2011, ApJ, 729, 145
Lada C. J., 1987, in Peimbert M., Jugaku J., eds, Proc. IAU Symp. 115, Star Forming Regions. Steward Observatory, Tucson, AZ, p. 1
Leggett S. K. et al., 2003, MNRAS, 345, 144
Lenzen R. et al., 2003, in Iye M., Moorwood A. F. M., eds, Proc. SPIE Conf. Ser. Vol. 4841, Instrument Design and Performance for Optical/Infrared Ground-based Telescopes. SPIE, Bellingham, p. 944
Liu Y., Madlener D., Wolf S., Wang H., Ruge J. P., 2012, A&A, 546, A7
Lucy L. B., 1999, A&A, 344, 282
Luhman K. L., Allen P. R., Espaillat C., Hartmann L., Calvet N., 2010, ApJS, 186, 111
Madlener D., Wolf S., Dutrey A., Guilloteau S., 2012, A&A, 543, A81
Marti J., Rodriguez L. F., Reipurth B., 1993, ApJ, 416, 208
Mather J. C., 2010, in Whalen D. J., Bromm V., Yoshida N., eds, AIP Conf. Ser., 1294, 1
Mathis J. S., Rumpl W., Nordsieck K. H., 1977, ApJ, 217, 425
Mie G., 1908, Ann. Phys., 330, 377
Mundt R., Buehrke T., Fried J. W., Neckel T., Sarcander M., Stocke J., 1984, A&A, 140, 17
Natta A., Testi L., Calvet N., Henning T., Waters R., Wilner D., 2007, in Reipurth B., Jewitt D., Keil K., eds, Protostars and Planets V. Antonella Natta, Osservatorio Astrofisico di Arcetri, p. 767
Padgett D. L., Brandner W., Stapelfeldt K. R., Strom S. E., Terebey S., Koerner D., 1999, AJ, 117, 1490
Pety J., Gueth F., Guilloteau S., Dutrey A., 2006, A&A, 458, 841
Pinte C. et al., 2008, A&A, 489, 633
Reipurth B., Chini R., Krugel E., Kreysa E., Sievers A., 1993, A&A, 273, 221
Rousset G. et al., 2003, in Wizinowich P. L., Bonaccini D., eds, Proc. SPIE Conf. Ser. Vol. 4839, Adaptive Optical System Technologies II. SPIE, Bellingham, p. 140
Sauter J. et al., 2009, A&A, 505, 1167
Shakura N. I., Sunyaev R. A., 1973, A&A, 24, 337
Siess L., Dufour E., Forestini M., 2000, A&A, 358, 593

Simon M., Chen W. P., Howell R. R., Benson J. A., Slowik D., 1992, ApJ, 384, 212
Stark D. P., Whitney B. A., Stassun K., Wood K., 2006, ApJ, 649, 900
Stokes G. G., 1852, Phil. Trans. R. Soc. I, 142, 463
Thompson R. I., Rieke M., Schneider G., Hines D. C., Corbin M. R., 1998, ApJ, 492, L95
Toomre A., 1964, ApJ, 139, 1217
Weingartner J. C., Draine B. T., 2001, ApJ, 548, 296
White R. J., Hillenbrand L. A., 2004, ApJ, 616, 998
Whitney B. A., Indebetouw R., Bjorkman J. E., Wood K., 2004, ApJ, 617, 1177
Wolf S., 2003a, Comp. Phys. Commun., 150, 99
Wolf S., 2003b, ApJ, 582, 859
Wolf S., Voshchinnikov N. V., 2004, Comp. Phys. Commun., 162, 113
Wolf S., Henning T., Stecklum B., 1999, A&A, 349, 839
Wolf S., Padgett D. L., Stapelfeldt K. R., 2003, ApJ, 588, 373
Yokogawa S., Kitamura Y., Momose M., Asaki Y., Tamura M., Ida S., Kawabe R., 2001, ApJ, 552, L59
Yokogawa S., Kitamura Y., Momose M., Kawabe R., 2002, in Ikeuchi S., Hearnshaw J., Hanawa T., eds, Proc. IAU Symp. II, 8th Asian-Pacific Regional Meeting. The Graduate University of Advanced Studies, Japan, p. 239

APPENDIX: PHOTOMETRIC DATA FOR FS TAU B

The photometric data points of FS Tau B are summarized in Table A1.

Table A1. Photometric data points for FS Tau B which are considered in the disc modelling (top) or are rejected (bottom).

$\lambda[\mu m]$	F_ν[mJy]	σ[mJy]	Instrument	Ref.
0.55	0.0354	0.0034	*WFPC2/HST*	(a)
0.7	0.0456	0.0044	*WFPC2/HST*	(a)
0.9	0.118	0.012	*WFPC2/HST*	(a)
1.1	0.77	0.03	*NICMOS/HST*	(b)
1.6	5.79	0.11	*NICMOS/HST*	(b)
1.87	10.9	0.2	*NICMOS/HST*	(b)
2.05	14.6	0.1	*NICMOS/HST*	(b)
2.159	12.8	1.28	*QUIRC/MKO*	(c)
3.6	42.116	3.939	*IRAC/SST*	(d)
3.74	53.6	1.1	*NACO/VLT*	(e)
4.5	83.587	3.123	*IRAC/SST*	(d)
5.8	154.499	9.447	*IRAC/SST*	(d)
8.0	276.857	16.929	*IRAC/SST*	(d)
11.56	429.0	2.491	*IRS/SST*	(f)
16.356	946.084	3.359	*IRS/SST*	(f)
24.0	1776	172	*MIPS/SST*	(f)
31.597	2502.883	7.235	*IRS/SST*	(f)
37.186	3046.1	26.807	*IRS/SST*	(f)
1300	141	13	*MPIfRBS/SEST*	(g)
2000	36	8	*NMA*	(h)
2126	36.7	2.6	*NMA*	(i)
2700	22	3	*PdBI/IRAM*	(j)
Not considered in the disc modelling:				
2×10^4	0.684	0.123	*VLA*	(k)
6×10^4	0.159	0.108	*VLA*	(k)

Notes. (a) Krist et al. (1998); (b) Padgett et al. (1999); (c) Connelley, Reipurth & Tokunaga (2007); (d) Luhman et al. (2010); (e) this work; (f) Furlan et al. (2011); (g) Reipurth et al. (1993); (h) Kitamura et al. (2002); (i) Yokogawa et al. (2001); (j) Dutrey et al. (1996); (k) Brown, Drake & Mundt (1986).

This paper has been typeset from a TEX/LATEX file prepared by the author.